

Plasma-Enhanced Atomic Layer Deposition Assisted Low-Temperature Synthetic Routes to Rationally Designed Metastable c-Axis Aligned Hexagonal In-Zn-O

TaeHyun Hong,[#] Hyeon Woo Kim,[#] Yoon-Seo Kim, Hyun-Jun Jeong, Sung Beom Cho,* and Jin-Seong Park*



Cite This: *Chem. Mater.* 2023, 35, 5168–5176



Read Online

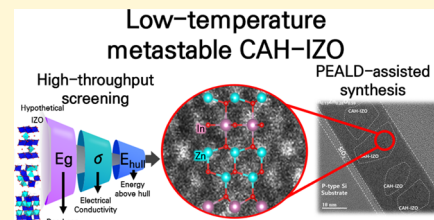
ACCESS |

Metrics & More

Article Recommendations

Supporting Information

ABSTRACT: Efforts to design and realize exotic metastable phases with advanced characteristics have been ongoing. However, the challenge lies in identifying their atomic structures and synthetic routes, as most explorations of metastability have relied on intuitions and trial-and-error approaches. Here, we present a computational workflow based on density functional theory (DFT) to rationalize the design of metastable materials. We demonstrate that plasma-enhanced atomic layer deposition (PEALD) is a profitable method for synthesizing target material. By screening the various hypothetical crystal structures of IZO compounds, we have identified the c-axis aligned hexagonal (CAH) $\text{In}_2\text{Zn}_4\text{O}_7$ as a promising candidate due to its metastability and superior electrical properties compared to a binary metal oxide system. Remarkably, this metastable phase can be synthesized at a significant temperature of 200 °C, compared to the typical crystallization temperature of the IZO system. This low-temperature crystallization is attributed to the distinctive features of PEALD, including tunable atomic order, precise composition control, and adjustable plasma source. By implementing CAH-IZO in thin-film transistor (TFT) applications, we observed desirable characteristics, such as a μFE of 43.4 cm²/V s, despite the low indium (In) content. We believe that this combined approach of PEALD and computational processing can expedite the realization of novel metastable materials, with the potential to expand their applications beyond traditionally explored materials.



1. INTRODUCTION

Metastable phases—kinetically trapped states despite their positive free energy above the ground state—are ubiquitous in nature.^{1,2} They sometimes exhibit fascinating properties that are not present in the stable or amorphous phase, so realizing metastable phases is emerging as a promising avenue for innovations in materials science. However, design and synthesis for the novel metastable phase are extremely challenging because most of the explorations for metastability have relied on experience, intuition, or even speculative predictions, namely “rules of thumb”.^{3–6} To overcome this limitation, the computational approach for identifying novel metastable phases has received the most attention due to its cost-effective and theoretically predictable advantages beyond traditional “Edisonian” trial-and-error searches.^{7–13} The computational approach can indicate promising candidates for the metastable phase. However, developing synthetic routes still requires human intuition and many trial-and-error routines. Recently, hydrothermal synthesis,¹⁴ solid-state reaction,^{15,16} and sputtering¹⁷ showed demonstrations for synthesizing a computationally designed metastable phase. Those synthetic approaches, on the other hand, still have unknown reaction paths, making stoichiometry control difficult and requiring a specific thermodynamic driving force to obtain the metastable state.

Atomic layer deposition (ALD), which enables atomistic designs by simultaneously controlling the scale and the stoichiometry of thin films, is considered a powerful tool to fabricate multicomponent materials for energy, catalyst, and transistor applications.^{18,19} Furthermore, ALD can select the oxidation state of cations through its versatile precursors and can additionally contribute to the extra thermodynamic driving force by applying the plasma source. Thus, it is a feasible route toward seizing the metastable state. In this regard, Wheeler et al. reported that metastable α -, ε -, and κ - Ga_2O_3 films were successfully controlled beyond the most stable β phase using plasma-enhanced atomic layer deposition (PEALD), and they demonstrated that metastable phases exhibited unique characteristics such as larger bandgaps, potential alloying for dopant and band-engineering and polarization.²⁰ Beyond the mono metal oxide, the realization of metastable multicomponent oxides was also emphasized, especially since the

Received: April 17, 2023

Revised: June 12, 2023

Published: June 26, 2023



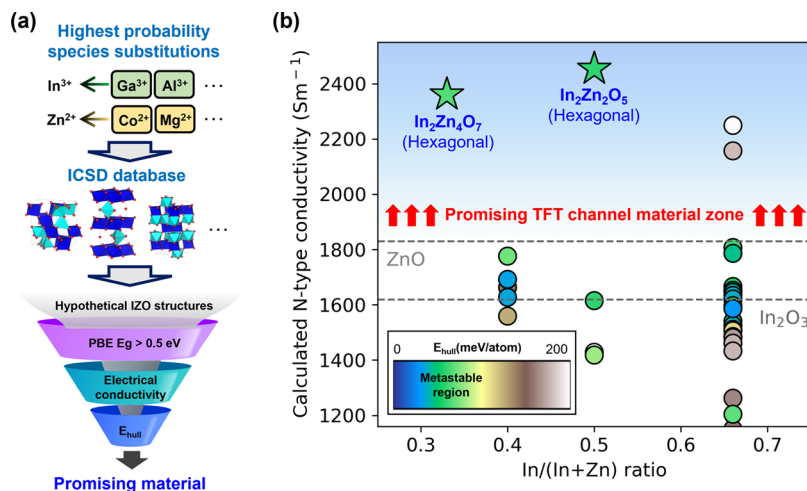


Figure 1. (a) Computational workflow for targeting promising In-Zn-O systems and (b) calculated n-type conductivity and energy above hull of hypothetical In-Zn-O binary metal oxide compounds.

binary or even ternary metal oxide systems are required for thin-film transistors (TFT), which are a key application of oxide semiconductors.^{16,21}

From a material point of view, oxide semiconductors are required to have high mobility and reliability, and several materials have been explored including IGZO,^{22–24} IGO,^{25–27} ITZO,^{28–30} and IZO.^{31–33} Among them, IZO is well-known as a candidate material that has high mobility and appropriate carrier concentration because it is composed of In_2O_3 and ZnO , each an n-type material. However, IZO thin films are generally reported as an amorphous phase because each In_2O_3 and ZnO has a distinct ground-state crystal structure (cubic and wurtzite, respectively) formed by different metal ionic sizes and charges. Due to these characteristics, previous reports used an extremely one-sided composition (In-rich or Zn-rich)³⁴ or used high-temperature ($>800^\circ\text{C}$)³⁵ annealing process to polycrystalline IZO. However, polycrystalline crystal is generally known which has defect states induced by grain boundary, and the high-temperature process is not suitable for the device application process.

In this work, we combine density functional theory (DFT) calculations and PEALD for the rational design of the metastable binary metal oxide by adopting In-Zn-O systems as a model case. We performed high-throughput DFT screening for the discovery of the novel IZO compounds and propose energetically metastable c-axis aligned hexagonal (CAH) $\text{In}_2\text{Zn}_4\text{O}_7$ as a promising binary metal oxide system for optoelectronic applications with the superior n-type conductivity to the mono metal oxide systems. We employed PEALD to assess the feasibility of forming CAH structures by fabricating $\text{In}_{0.13}\text{Zn}_{0.28}\text{O}_{0.59}$ thin films and identified its successful synthesis by X-ray diffraction (XRD) and transmission electron microscopy (TEM). By calculating the enthalpy of mixing, we showed that the energy of the CAH structure in the IZO alloys is lowest at an In/(In + Zn) ratio of 0.33, making it possible to understand why crystallization occurred in $\text{In}_{0.13}\text{Zn}_{0.28}\text{O}_{0.59}$ thin films. Finally, to examine the potential of the device application, inverted staggered-type TFTs were fabricated using PEALD-based IZO as an active layer. The TFT exhibited high mobility ($43.4 \text{ cm}^2/\text{V s}$) and a low S.S value (0.22 V/decade) at the CAH structure of IZO.

2. RESULTS AND DISCUSSION

2.1. Rational Design for Metastable IZO via Exploring the Hypothetical Chemical Compound. Figure 1a shows our workflow to design the metastable IZO compound based on ionic substitution, data mining on crystal structures, and DFT-based thermodynamics. The idea of rational design involves substituting ions for already-known crystal structures (prototype structures) and calculating its thermodynamic stability. First, we considered “commensurate” cations with In^{3+} and Zn^{2+} , which have high substitution probability considering the ionic radius, oxidation states, and other elemental properties.³⁶ This approach is also based on leveraging large databases of known compounds; thereby, it is possible to explore statistically plausible alternatives to the original ion swiftly. Based on all the possible commensurate cation combinations, we then data-mined the already-known oxide crystal structures from ICSD³⁷ and other DFT-based databases.³⁸ By substituting cations with In^{3+} or Zn^{2+} from the crystal structures, we generated hypothetical candidates for metastable IZO compounds. For instance, ions with the highest substitution probability for In^{3+} in the IZO system were identified as Al^{3+} and Ga^{3+} (Figure S1), and the crystal structure observed in both Al-Zn-O and Ga-Zn-O compounds can be considered as a prototype structure for new IZO binary metal oxide compounds. Beyond the binary metal oxide system, we further explored prototypes by data-mining ternary metal oxides containing In and Zn in Material Project³⁸ and then substituted them with original ions. By integrating the compounds collected via the above methods, 270 hypothetical IZO structures with distinct configurations were obtained, all of which were computed by DFT calculations.

We extracted the calculated band gap and electrical conductivity from DFT calculation results and used them as descriptors, which can carry out a screening process to explore promising IZO candidates. For the electrical conductivity, we used the BoltzTraP³⁹ package, which can compute the electrical transport properties of materials by taking into account the electronic band structure and the scattering mechanisms. We start the set of descriptor criteria by considering the calculated electrical properties of In_2O_3 and ZnO since our goal is to find a better ternary system than binary systems.²¹ We identified that the calculated electrical

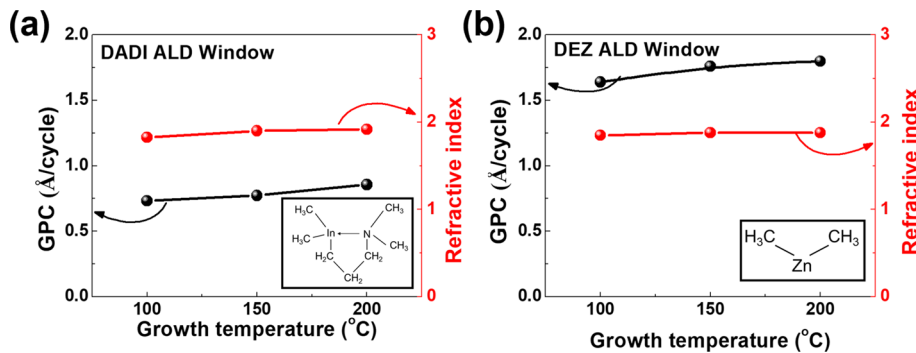


Figure 2. GPC and RI of ALD (a) In_2O_3 and (b) ZnO for different growth temperatures from 100 to 200 $^{\circ}\text{C}$ using DADI and DEZ precursors, respectively.

Table 1. Thin-Film Composition Ratio of $\text{In}_x\text{Zn}_y\text{O}_z$ According to the In_2O_3 , ZnO Subcycles

$\text{In}_2\text{O}_3(n_1)$ - $\text{ZnO}(n_2)$ *ALD cycle	C%	N%	In%	Zn%	O%	In/Zn
$\text{In}_2\text{O}_3(1)$ - $\text{ZnO}(3)$	N/A	N/A	4.9 ± 0.2	38.1 ± 0.1	57.0 ± 0.2	0.11:0.89
$\text{In}_2\text{O}_3(3)$ - $\text{ZnO}(1)$	N/A	N/A	13.3 ± 0.3	27.8 ± 0.2	58.9 ± 0.3	0.32:0.68
$\text{In}_2\text{O}_3(6)$ - $\text{ZnO}(1)$	N/A	N/A	17.6 ± 0.2	22.8 ± 0.3	59.6 ± 0.3	0.44:0.56
$\text{In}_2\text{O}_3(36)$ - $\text{ZnO}(1)$	N/A	N/A	25.4 ± 0.4	11.7 ± 0.2	62.9 ± 0.2	0.68:0.32

properties, which are the band gap and n-type conductivity, are 0.92 eV with 1620 S m^{-1} for In_2O_3 and 0.72 eV with 1830 S m^{-1} for ZnO , respectively. Then, we used the band gap >0.5 eV and the N-type conductivity $>1830 \text{ S m}^{-1}$ as the screening conditions. Furthermore, we confirm metastable compounds by calculating energy above hull within 100 meV/atom. This limit is set by the metastable limit suggested by Sun et al.¹ Note that this limit is not absolute in terms of synthesizability, as it can vary depending on the materials class. Figure 1b shows that $\text{In}_2\text{Zn}_4\text{O}_7$ and $\text{In}_2\text{Zn}_2\text{O}_5$ compounds are promising candidates as a TFT channel material, exhibiting metastability in the IZO system. For both, the energy above hull was calculated to be 66 and 81 meV/atom, and the calculated n-type conductivity was predicted to be 2361 and 2479 S m^{-1} , respectively. These n-type conductivity values were comparatively high compared to other oxides within a similar class, as shown in Figure S2. We also identified the atomic structure of the candidates to provide insight into the experimental synthesis, as shown in Figure S3. The atomic structure of $\text{In}_2\text{Zn}_4\text{O}_7$ was similar to that of CAAC IGZO,⁴⁰ which was recently synthesized by ALD.⁴¹ This implies that the appropriate synthetic route for $\text{In}_2\text{Zn}_4\text{O}_7$ can be achieved by ALD. Therefore, we focused more on the $\text{In}_2\text{Zn}_4\text{O}_7$ among the two candidates and proposed ALD to synthesize it.

2.2. Synthesis of $\text{In}_x\text{Zn}_y\text{O}_z$ Thin Films via PEALD and Investigating Thin-Film Properties. Before synthesizing multicomponent metal oxide using ALD, each $\text{In}_2\text{O}_3/\text{ZnO}$ ALD process (which uses separate precursors and reactants) should be investigated. The saturated growth per cycle (GPC) was observed in the range of 100 to 200 $^{\circ}\text{C}$ according to both the In_2O_3 and ZnO ALD processes using each DADI ([3-(dimethylamino)propyl]dimethyl indium), DEZ (diethyl zinc) precursor (Figure 2). The IZO PEALD process was performed at 200 $^{\circ}\text{C}$, which is the highest temperature ALD window, to offer sufficient energy during synthesis, and the ALD sequential technique, which was composed of $[(\text{In}_2\text{O}_3) \times n_1 \text{ cycles} - (\text{ZnO}) \times n_2 \text{ cycles}]$, was used to adjust the composition fraction of IZO (the schematic of ALD IZO process is shown in Figure S5). In Figure S6, we compare the actual GPC and the calculated GPC of IZO based on the cycles and subcycles.

We confirmed that unexpected growth (such as nucleation effects during the multicomponent ALD process) did not occur.

To investigate the chemical composition of the ALD IZO, XPS analysis was conducted and is presented in Table 1. Impurities such as carbon and nitrogen were not observed. The metal element ratio was represented in the form of In/Zn. With increasing ALD In_2O_3 subcycles, the In-composition fraction can be controlled from 0.11 to 0.68, and we denoted each thin film as follows: $\text{In}_{0.05}\text{Zn}_{0.38}\text{O}_{0.57}$, $\text{In}_{0.13}\text{Zn}_{0.28}\text{O}_{0.59}$, $\text{In}_{0.17}\text{Zn}_{0.23}\text{O}_{0.60}$, and $\text{In}_{0.25}\text{Zn}_{0.12}\text{O}_{0.63}$. It should be noted that the compositions of $\text{In}_{0.13}\text{Zn}_{0.28}\text{O}_{0.59}$ and $\text{In}_{0.17}\text{Zn}_{0.23}\text{O}_{0.60}$ are similar to $\text{In}_2\text{Zn}_4\text{O}_7$ and $\text{In}_2\text{Zn}_2\text{O}_5$, respectively, which were introduced in the previous section as being the metastable candidate group.

In this regard, we conducted XRD analysis to investigate the atomic structure of deposited IZO thin films, as shown in Figure 3. ALD IZO thin films were observed for four different crystal structures concerning the metal composition fraction. It should be noted that $\text{In}_{0.13}\text{Zn}_{0.28}\text{O}_{0.59}$ showed a single XRD peak despite the low-temperature process of 200 $^{\circ}\text{C}$ and the composition of In and Zn being moderately mixed. The

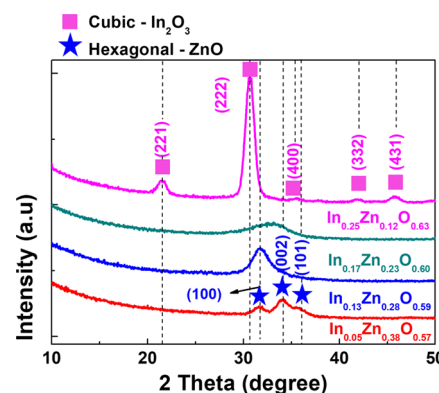


Figure 3. XRD data for $\text{In}_x\text{Zn}_y\text{O}_z$ with respect to the In/Zn composition ratio.

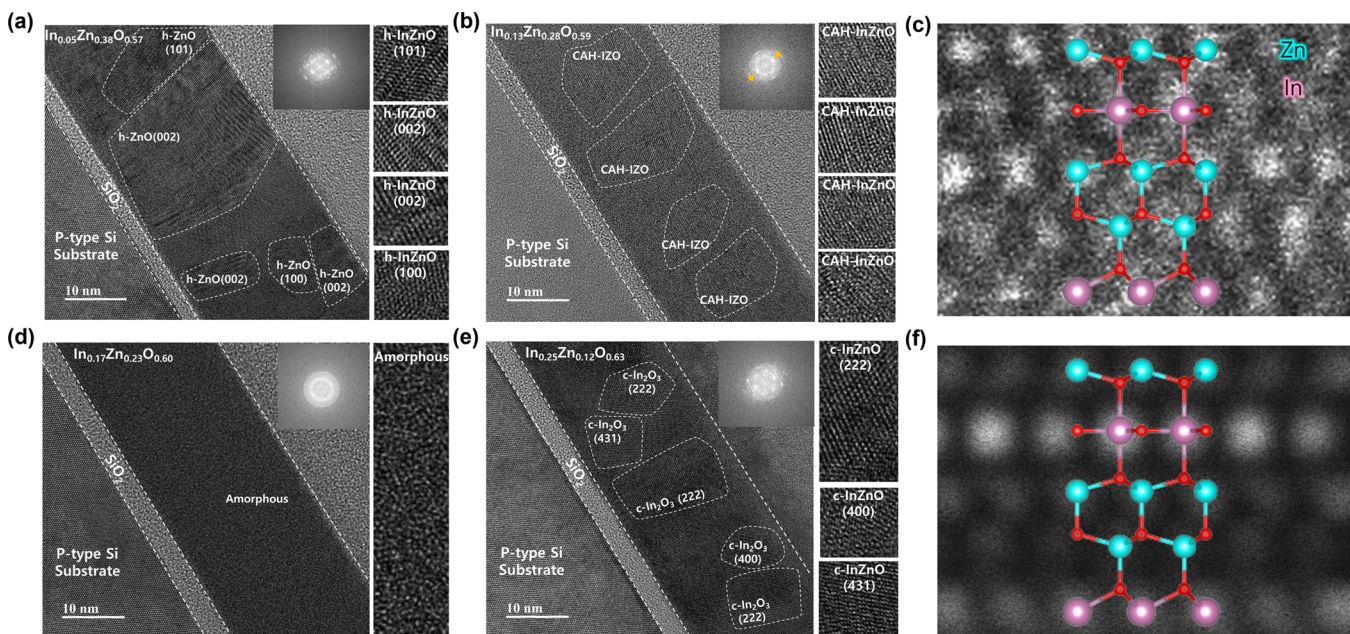


Figure 4. HR-TEM images of $\text{In}_x\text{Zn}_y\text{O}_z$ films deposited with different X/Y ratios of (a) $\text{In}_{0.05}\text{Zn}_{0.38}\text{O}_{0.57}$, (b) $\text{In}_{0.13}\text{Zn}_{0.28}\text{O}_{0.59}$, (d) $\text{In}_{0.17}\text{Zn}_{0.23}\text{O}_{0.60}$, and (e) $\text{In}_{0.25}\text{Zn}_{0.12}\text{O}_{0.63}$ (the insets show the corresponding FFT patterns). Images of CAH-IZO overlapped on (c) HAADF-STEM and (f) QSTEM, respectively.

$\text{In}_{0.05}\text{Zn}_{0.38}\text{O}_{0.57}$ thin film, which has an Zn-rich film, shows clear hexagonal-ZnO (h-ZnO) peaks at 31.7° , 34.4° , and 36.2° of 2θ corresponding to (100), (002), and (101) planes, respectively (JCPS card # 79-0207). As an In-rich IZO, $\text{In}_{0.25}\text{Zn}_{0.12}\text{O}_{0.63}$ shows a cubic- In_2O_3 (c- In_2O_3) crystal structure (JCPS card # 76-0152). This implies that if one element increases over a specific amount, it acts as a dominant material, resulting in a preference for its crystalline phase. We also observed the XRD spectra for two other compositions, which are candidates that can have a metastable phase as mentioned in the DFT calculation section. $\text{In}_{0.17}\text{Zn}_{0.23}\text{O}_{0.60}$ exhibited an amorphous phase, while the DFT-predicted hexagonal- $\text{In}_2\text{Zn}_2\text{O}_5$ did not appear. We noted that the PEALD-based synthesis of $\text{In}_2\text{Zn}_2\text{O}_5$ is still obscure, suggesting that further study into synthetic routes is necessary. On the other hand, another candidate, $\text{In}_{0.13}\text{Zn}_{0.28}\text{O}_{0.59}$, has an exclusive structure with a clear XRD peak at 31.7° corresponding to h-ZnO (100) despite the decrease in the fraction of Zn. Since the unit cell of CAH-IZO is composed of alternating aligned wurtzite-ZnO layers and InO_x layers, this could be misinterpreted that the hexagonal structure is due to the ZnO layer. Furthermore, we confirmed that this phase can be maintained under the annealing process even after heating at 600°C for 3 h in an ambient atmosphere. The crystallinity and XPS analysis according to the annealing temperature were investigated, as presented in Figure S7 and Table S1, respectively. Although the relatively volatile Zn was slightly reduced in the 600°C high-temperature annealing process, the CAH-IZO crystal phase maintained stable, and it will be discussed further in the DFT calculation.^{42,43}

To further analyze the microstructures of as-deposited thin films, TEM analysis was performed on the four different IZO compositions (each HR-TEM image and Fast Fourier transform (FFT) are presented in Figure 4a,b and d,e). The clear lattice fringes of h-ZnO structure with (100), (002), and (101) lattice plane parameters of 2.82, 2.63, and 2.49 Å were observed over the whole region of $\text{In}_{0.05}\text{Zn}_{0.38}\text{O}_{0.57}$ thin film, as

presented in Figure 4a. As a metastable structure, the $\text{In}_{0.13}\text{Zn}_{0.28}\text{O}_{0.59}$ shows a CAH structure, with the only lattice plane parameters of 2.82 Å (Figure 4b), and the corresponding atomic structure from DFT (Figure S8). In addition, the crystal structure was formed on an atomically flat plane over the whole region. For the $\text{In}_{0.17}\text{Zn}_{0.23}\text{O}_{0.60}$, the amorphous HR-TEM image was observed as well as diffused ring-pattern of FFT as presented in Figure 4d, which is consistent with the XRD analysis. The microstructure of $\text{In}_{0.25}\text{Zn}_{0.12}\text{O}_{0.63}$ shows a polycrystalline cubic structure, in which the (222), (400), and (431) planes of c- In_2O_3 were measured to be 2.92, 2.53, and 1.98 Å, respectively (Figure 4e).

To confirm the atomic structure of $\text{In}_{0.13}\text{Zn}_{0.28}\text{O}_{0.59}$ in more detail, we performed high-angle annular dark field scanning transmission electron microscopy (HAADF-STEM) as presented in Figure 4c. The expected CAH atomic structure is clearly revealed in the HAADF-STEM image, and the unit cells are labeled for comparison. Then, a simulated STEM image of CAH-In₂Zn₄O₇ was extracted by a quantitative STEM (QSTEM) package⁴⁴ using the atomic structure derived from the DFT calculation, and the atomic structure is labeled in Figure 4f. The HAADF image exhibits excellent agreement with the atomic structure and QSTEM image of CAH-In₂Zn₄O₇. Furthermore, to confirm the metal distribution of as-deposited thin film, an EDS analysis was conducted, shown in Figure S9. As shown in Figure S9a-d, all IZO thin films were deposited with homogeneous mixing, which has no interface layer for either In_2O_3 or ZnO.

2.3. Understanding the Formation of CAH IZO. The enthalpy of mixing, which allows for the direct prediction of alloy phase stability from the DFT calculations under equal stoichiometry, can illustrate the energetic stability against composition fluctuations.^{8,45} For the IZO system, the stoichiometry is nonequal due to the difference in the oxidation number of the cations with In^{3+} and Zn^{2+} , causing oxygen deficiency/excess.⁴⁶ Therefore, the enthalpy of mixing for wurtzite IZO alloys was defined as

$$\Delta H_{\text{mix}}[\text{In}_x\text{Zn}_{1-x}\text{O}] = E[\text{In}_x\text{Zn}_{1-x}\text{O}] - xE[\text{In}_2\text{O}_3] - (1-x)E[\text{ZnO}] + \frac{n}{2}\mu_{\text{O}_2}$$

where x is the molar concentration, $E[\text{In}_x\text{Zn}_{1-x}\text{O}]$ is the total energy of the SQS⁴⁷ supercell structure representing the random alloy, $E[\text{In}_2\text{O}_3]$ and $E[\text{ZnO}]$ are the total energies of In_2O_3 and ZnO in the ground state, n is the number of oxygen deficiency/excess, and μ_{O_2} is the oxygen chemical potential.

Total energies and chemical potential were obtained from the DFT calculations. This enthalpy of mixing can be fitted with the regular solution model for heterostructural alloy in the form of

$$\Delta H_{\text{mix}}(x) = x\Delta H_0 + (1-x)\Delta H_1 + x(1-x)\Omega$$

where H_0 and H_1 are the enthalpies of the endpoints for In_2O_3 and ZnO , respectively, and Ω is the regular solution interaction parameters, which are the bond energy (U) differences between unequal and equal atomic species $\Omega = 2U_{\text{InZn}} - U_{\text{InIn}} - U_{\text{ZnZn}}$. The fitted enthalpies of mixing and evaluated Ω are shown in Figure S10.

Based on the metastable limit, we also defined areas where preferred structures were discernible. Figure 5 shows the DFT-

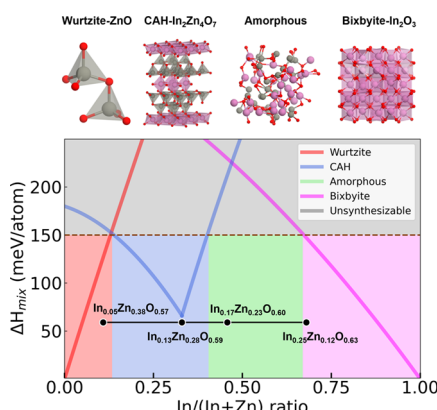


Figure 5. Calculated enthalpy of mixing in $\text{In}-\text{Zn}-\text{O}$ alloys as a function of the $\text{In}/(\text{In} + \text{Zn})$ ratio. The thermodynamic limit for synthesis was set to < 150 meV/atom suggested by Sun. The preference for an amorphous structure was mimicked if the structure of any alloy was energetically unfavorable.

calculated enthalpy of mixing as the function of the $\text{In}/(\text{In} + \text{Zn})$ ratio with our experimental results. We first confirmed the agreement between theoretical and experimental results. For the ground-state crystal structures of ZnO and In_2O_3 , the enthalpies of mixing were low at $\text{In}/(\text{In} + \text{Zn})$ ratios of less than 0.13 for wurtzite and more than 0.67 for bixbyite, respectively. These ranges include h-ZnO $\text{In}_{0.05}\text{Zn}_{0.38}\text{O}_{0.57}$ and c- In_2O_3 $\text{In}_{0.25}\text{Zn}_{0.12}\text{O}_{0.63}$ thin films as mentioned in the synthesis section. Additionally, we identified that CAH and amorphous structures, which contain thin films of $\text{In}_{0.13}\text{Zn}_{0.28}\text{O}_{0.59}$ and $\text{In}_{0.17}\text{Zn}_{0.23}\text{O}_{0.60}$, are preferred at $\text{In}/(\text{In} + \text{Zn})$ ratios of 0.13–0.41 and 0.41–0.67, respectively (the composition fraction of $\text{In}_{0.13}\text{Zn}_{0.28}\text{O}_{0.59}$ after annealing by 600 °C is also satisfied with the CAH composition range resulting from DFT calculation). This means that the DFT-predicted energetic stability against composition fluctuations is consistent with the IZO synthesized by PEALD.

We now focus on understanding the formation mechanism of the CAH-IZO and investigate why it could be synthesized using PEALD. First, the IZO system involves heterostructural alloys mixed with materials with different ground-state structures. This alloy often exhibits a peculiar behavior in which a metastable phase occurs if a specific ordering of the polyhedral is satisfied.^{48,49} In other words, it implies that the atomic layer sequence controlled by PEALD was compatible with the ordering of CAH-IZO. It is also noteworthy that the lowest point in the enthalpy of mixing for CAH-IZO, which is 66 meV/atom at the $\text{In}/(\text{In} + \text{Zn})$ ratio of 0.33, matches the CAH- $\text{In}_{0.13}\text{Zn}_{0.28}\text{O}_{0.59}$ thin film synthesized by PEALD. Since the sequential technique of ALD has properties both of composition control and the separate deposition of each oxide layer, it could be inducing the specific ordered atomic structures satisfying metal composition fraction of metastable IZO. Although the CAH structure has the lowest enthalpy value when the $\text{In}/(\text{In} + \text{Zn})$ ratio is 0.33, the required mixing enthalpy is over 66 meV/atom. We speculate that the extra plasma source could provide extra kinetic energy during the growth of the IZO thin film, driving the film toward metastable CAH structure. Thus, the formation of metastable CAH-IZO is possible due to the precise composition control capability and assisted plasma source of the PEALD.

Despite the particularly low range of enthalpy of mixing for CAH-IZO, it is noted that homogeneous IZO compounds could be synthesized within a wide composition range if the environment of synthesis 1250 °C,⁵⁰ which is higher than ours. On the other hand, the processing of oxide TFTs requires temperatures up to 350 °C, indicating that most of the synthesized thin films are amorphous. We emphasize here that the metastable CAH-IZO thin films can be synthesized at relatively low temperature (200 °C) through efforts to carefully control the composition as well as rationally apply plasma energy.

2.4. Thin-Film Properties of PEALD-IZO Thin Films and TFT Application. Hall measurements were performed to examine the electrical properties (hall mobility, carrier concentration, and resistivity) according to four $\text{In}_x\text{Zn}_y\text{O}_z$ thin films, as shown in Figure 6. Since the electrical properties are significantly influenced by metal composition fraction and crystallinity, it should be interpreted comprehensively.^{22,51,52} As the In-composition increases, the mobility could be increased through electron transport formation by overlapping spherical In 5s orbitals. However, the mobility of CAH-

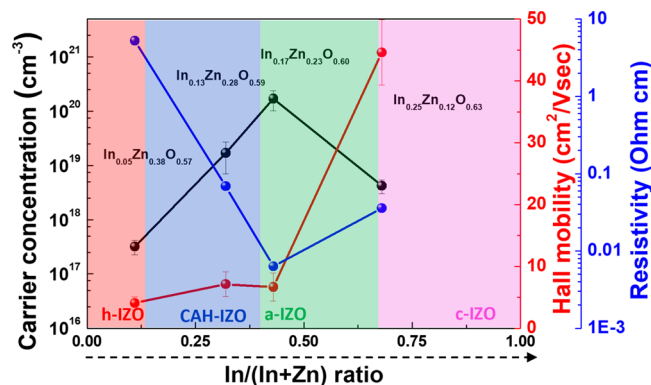


Figure 6. Hall measurement of $\text{In}_x\text{Zn}_y\text{O}_z$ films deposited with different X/Y ratios of $\text{In}_{0.05}\text{Zn}_{0.38}\text{O}_{0.57}$, $\text{In}_{0.13}\text{Zn}_{0.28}\text{O}_{0.59}$, $\text{In}_{0.17}\text{Zn}_{0.23}\text{O}_{0.60}$, and $\text{In}_{0.25}\text{Zn}_{0.12}\text{O}_{0.63}$.

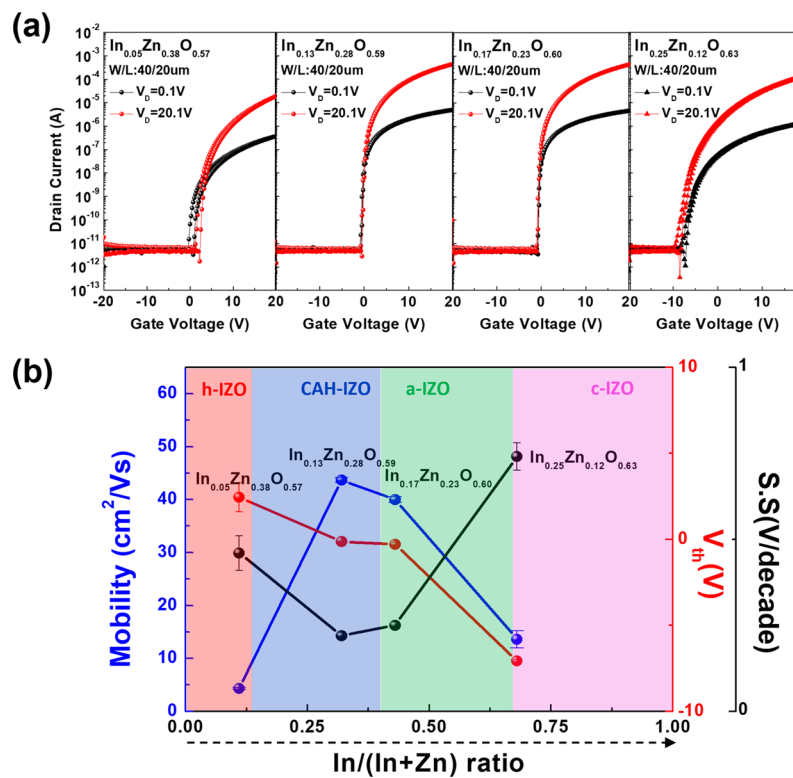


Figure 7. (a) Transfer curves of $\text{In}_x\text{Zn}_y\text{O}_z$ films deposited with different X/Y ratios. (b) Device parameters of V_{th} , mobility, and S.S. in terms of InO and ZnO subcycles.

$\text{In}_{0.13}\text{Zn}_{0.28}\text{O}_{0.59}$ was slightly higher than $\text{a-In}_{0.17}\text{Zn}_{0.23}\text{O}_{0.60}$ despite the lower In fraction. The crystalline materials, such as c-axis aligned structure, have ordered bond configurations compared to their amorphous counterparts. Furthermore, the bonding states in IZO are more stable with a lower variation. To understand this phenomenon in more detail, we calculated the conductivity and effective mass according to the crystal phase of IZO, as shown in Figure S11. The calculated effective mass, which significantly affected mobility,⁵³ exhibited the lowest value for a CAH-IZO structure (0.131) as compared to other structures. In addition, the calculated conductivity was highest at identical carrier concentrations. In $\text{In}_{0.25}\text{Zn}_{0.12}\text{O}_{0.63}$ thin films in which the In fraction was increased to 68%, the decreased carrier concentration and increased resistivity were observed, which was expected due to the grain boundaries, which formed via recrystallization from an amorphous phase. Since the amorphous thin film could have a relatively loose metal–oxygen bond, the highest carrier concentration in a $\text{In}_{0.17}\text{Zn}_{0.23}\text{O}_{0.60}$ may be obtained.

Finally, to examine the characteristics of a device with regard to each $\text{In}_x\text{Zn}_y\text{O}_z$ thin film, bottom-gate and top-contact device structures using PEALD IZO were fabricated and analyzed (the transfer curves and device performance are represented in Figure 7, and the TFT characteristics are summarized in Table S2). Device deterioration occurred in devices of both $\text{In}_{0.05}\text{Zn}_{0.38}\text{O}_{0.57}$ and $\text{In}_{0.25}\text{Zn}_{0.12}\text{O}_{0.63}$. That is, S.S. increased and μ_{eff} decreased rapidly due to defect sites created by grain boundaries of polycrystalline. In contrast, with crystalline phase alignment, the $\text{In}_{0.13}\text{Zn}_{0.28}\text{O}_{0.59}$ device show improved device properties with a high μ_{eff} ($43.4 \text{ cm}^2/\text{V s}$). The $\text{In}_{0.13}\text{Zn}_{0.28}\text{O}_{0.59}$ showed the smallest S.S. values (0.22 $\text{V}/(\text{decade})$), suggesting that the thin film of CAH-IZO had the lowest defect sites due to aligned crystallization.

It should be noted that the $\text{In}_{0.13}\text{Zn}_{0.28}\text{O}_{0.59}$ has higher μ_{eff} values due to a lower effective mass than that of $\text{In}_{0.17}\text{Zn}_{0.23}\text{O}_{0.60}$ despite to lower In fraction. In oxide semiconductor materials, a higher carrier concentration is generally reported to positively affect mobility since it could help overcome the potential barrier near the conduction band minimum (CBM).^{54,55} Based on this concept, further investigation of increased carrier concentration while maintaining CAH-IZO structures, such as hydrogen doping, is suggested for development.

3. CONCLUSIONS

In this article, we computationally targeted tailored and accessible metastable IZO compounds exhibiting moderate band gap and superior n-type conductivity than the mono metal oxide system. Subsequently, CAH- $\text{In}_{0.13}\text{Zn}_{0.28}\text{O}_{0.59}$ was successfully grown through the PEALD method at the temperature of 200 °C. In contrast to the typical crystallization temperature of In-Zn-O systems, we identified a low-temperature crystallization that can satisfy the constraint conditions in the oxide TFT process (<350 °C). The crystal structure of the as-deposited thin film exhibited a hexagonal structure with the c-axis based on XRD and TEM analysis, while c- In_2O_3 (polycrystalline), h- ZnO (polycrystalline), and amorphous phases appeared in other compositions of IZO. These results were consistent with calculated enthalpies of mixing of In-Zn-O systems as a function of the $\text{In}/(\text{In} + \text{Zn})$ ratio. $\text{In}_{0.13}\text{Zn}_{0.28}\text{O}_{0.59}$, which is a c-axis hexagonal structure, showed enhanced TFT characteristics even though the carrier concentration was not high due to a relatively low In composition fraction. It is noteworthy that the high mobility ($43.4 \text{ cm}^2/\text{V s}$) is due to low effective mass and improved S.S. (0.22 $\text{V}/(\text{decade})$) is due to low defect states. From this study,

we demonstrated the potential of searching for metastable materials through simulation and PEALD. We believe that this process can lead to establishing a novel route to functional materials that can be applied in a variety of systems.

4. EXPERIMENTAL SECTION/METHODS

4.1. IZO Thin-Film Deposition Techniques and Analyses.

IZO thin films were deposited using PEALD using DADI ([3-(dimethylamino)propyl]dimethyl indium) and DEZ (Diethylzinc) precursors for In_2O_3 and ZnO , respectively. Ar/O_2 plasma was used as the reactant, and a 1.2 Torr chamber pressure was maintained while igniting the plasma. To adjust the cation composition of IZO, the PEALD super-cycle was conducted, which consisted of $[(\text{In}_2\text{O}_3) \times n_1 \text{ cycles} - (\text{ZnO}) \times n_2 \text{ cycles}]$, where (n_1, n_2) is $(1, 3)$, $(3, 1)$, $(6, 1)$, and $(36, 1)$. Spectroscopic ellipsometry (SE; Ellipso Technology, UV-FMS) was used to measure the thickness and refractive index of the as-deposited oxide thin film. The chemical composition of the as-deposited IZO was investigated by X-ray photoelectron spectroscopy (XPS, K-alpha+, Thermo Fisher Scientific Co). Each chemical composition exhibited an average of evaluated samples ($n = 6$) for each process. The crystallinity of IZO thin films (30 nm) was measured by grazing incidence X-ray diffraction (GIXRD, SmartLab, Rigaku Co) using a Cu $\text{K}\alpha$ X-ray ($\lambda = 1.5406 \text{ \AA}$) source. High-resolution transmission electron microscopy (HRTEM, JEM-2100F, JEOL) was used to examine the IZO thin film's microstructure. The optical bandgap of $\text{In}_x\text{Zn}_y\text{O}_z$ thin films was evaluated by Tauc plots using transmittance of thin films measured through UV-visible spectroscopy (Figure S12). The film density of as-deposited IZO was analyzed by X-ray reflectivity (XRR, SmartLab, Rigaku Co) as shown in Figure S13.

4.2. Fabrication and Characteristics of Oxide TFTs Based on IZO.

To fabricate the bottom-gate and top-contact structure, 20 nm-thick IZO was grown on a thermally oxidized SiO_2 (100 nm)/ P^{++} substrate. The IZO active layer was patterned through conventional photolithography and a wet-etching process. As an electrode, indium tin oxide (ITO) of 100 nm was deposited by radiofrequency (RF) magnetron sputtering, and the lift-off process was performed to avoid chemical damage on the active layer if using a wet-etching method. The devices were annealed at 400°C in an ambient atmosphere for 3 h. The channel width (W) and length (L) of the active layer were defined as 40 and 20 μm , respectively. A Keithley 4200 analyzer was used to examine the electrical properties of the TFTs, and the transfer curve was evaluated using a gate voltage sweep from -20 to 20 V at drain voltages of 0.5 and 15.5 V, respectively.

4.3. High-Throughput DFT Calculation of Hypothetical Chemical Compounds. DFT calculations for the 270 hypothetical IZO compounds were performed with the Vienna ab initio software package (VASP)^{56,57} using the projector augmented-wave method⁵⁸ with the generalized gradient approximation (GGA) within the Perdew–Burke–Ernzerhof (PBE) framework.⁵⁹ The plane-wave basis set was expanded to a cutoff energy of 520 eV, which was 1.3 times the maximum cutoff as specified by the VASP pseudopotentials. The structural optimization was truncated until the Hellmann–Feynman forces were under 0.01 eV/ \AA . Electronic energy convergence was set to $1 \times 10^{-5} \text{ eV}$. The Brillouin zone was sampled using 100 k -points density per inverse \AA^3 of reciprocal cell. Band gap and energy above hull were extracted using Python Materials Genomics (PyMatGen) package.⁶⁰ A self-consistent static calculation was performed with the Brillouin zone sampled by 1000 k -points density per inverse \AA^3 of reciprocal cell. The n-type electrical conductivity was calculated using the BolzTraP³⁹ package at a doping level of 10^{18} cm^{-3} and at a temperature of 300 K. These values were used in the previous high-throughput calculation.⁶¹

4.4. Calculation of Disordered Crystalline IZO Alloys.

Disordered IZO alloys were computed using 64 atoms for wurtzite, 320 atoms for bixbyite, and 208 atoms for hexagonal $\text{In}_2\text{Zn}_4\text{O}_7$ structures. To simulate random alloys based on special quasi-random structures (SQS),⁶² we used the mcsqs code of the Alloy Theoretic Automated Toolkit (ATAT).⁶³ The $\text{In}/(\text{In} + \text{Zn})$ ratio of wurtzite

and bixbyite alloys was sampled at 0.25, 0.50, and 0.75, and that of the hexagonal $\text{In}_2\text{Zn}_4\text{O}_7$ alloy was additionally sampled at 0.125 and 0.625. The Brillouin zone was sampled using the Gamma-centered method with $2 \times 2 \times 3$ k -points for wurtzite, $2 \times 2 \times 2$ k -points for bixbyite, and $3 \times 3 \times 1$ k -points for hexagonal $\text{In}_2\text{Zn}_4\text{O}_7$ structures.

4.5. HAADF-STEM Image Simulation by QSTEM.

The HAADF-STEM image simulation was performed using the QSTEM⁴⁴ simulation software. The atomic structure model of CAH- $\text{In}_2\text{Zn}_4\text{O}_7$ consisting of $7 \times 10 \times 2$ unit cells was used in the simulations. The sample was tilted 90° along the Y-axis. The probe array was 60×60 pixels with 0.05 \AA the resolution. The slice thickness was 1.3739 \AA . The image simulations were performed for an XY area corresponding to $X = 31.5\text{--}50 \text{ \AA}$ and $Y = 0\text{--}20 \text{ \AA}$ with 19×22 pixels. The microscope parameters for QSTEM were as follows: 200 kV high voltage; -13.7 nm defocus; 0.05 mm astigmatism spherical aberration, C3; 15 mrad convergence angle; 5×10^8 brightness ($\text{A cm}^{-2} \text{ sr}^{-1}$); TDS on; 0.6 eV de; 1 μs dwell time; 300 K temperature; 0° angle; and 0° beam tilt. The values for detector geometry were 70 to 133 mrad.

■ ASSOCIATED CONTENT

Data Availability Statement

The data that support the findings of this study are available from the corresponding author upon reasonable request.

Supporting Information

The Supporting Information is available free of charge at <https://pubs.acs.org/doi/10.1021/acs.chemmater.3c00894>.

$\text{In}_{0.13}\text{Zn}_{0.28}\text{O}_{0.59}$ thin-film composition after annealing at 400 and 600°C for 3 h investigated by XPS; device performances of $\text{In}_x\text{Zn}_y\text{O}_z$ films deposited with different X/Y ratios of $\text{In}_{0.05}\text{Zn}_{0.38}\text{O}_{0.57}$, $\text{In}_{0.13}\text{Zn}_{0.28}\text{O}_{0.59}$, $\text{In}_{0.17}\text{Zn}_{0.23}\text{O}_{0.60}$, and $\text{In}_{0.25}\text{Zn}_{0.12}\text{O}_{0.63}$; predicted ion substitution probability for In-Zn-O systems; transport properties of other crystalline oxides relevant to TFT channel materials; atomic structure of metastable IZO compounds and C-axis aligned hexagonal structure of IGZO; number of hypothetical crystal structures according to the crystal system; the calculated PBE band gap versus Ehull in In-Zn-O systems; PEALD InZnO process cycle using DADI & DEZ precursors; calculated GPC and actual GPC according to the In_2O_3 , ZnO subcycle ratio of $\text{In}_x\text{Zn}_y\text{O}_z$; XRD data for $\text{In}_x\text{Zn}_y\text{O}_z$ after annealing at 400°C for 3 h and 600°C for 3 h with respect to the In/Zn composition ratio; C-axis lattice parameter of CAH-IZO in the a-axis view; energy dispersive spectroscopy mapping of the elemental distributions of In, Zn, O, and Si with respect to $\text{In}_{0.05}\text{Zn}_{0.38}\text{O}_{0.57}$, $\text{In}_{0.13}\text{Zn}_{0.28}\text{O}_{0.59}$, $\text{In}_{0.17}\text{Zn}_{0.23}\text{O}_{0.60}$, and $\text{In}_{0.25}\text{Zn}_{0.12}\text{O}_{0.63}$; calculated enthalpy of mixing of IZO alloys for wurtzite, bixbyite, and $\text{In}_2\text{Zn}_4\text{O}_7$ structures; calculated conductivity and effective mass of wurtzite ZnO , c-axis aligned hexagonal $\text{In}_2\text{Zn}_4\text{O}_7$ (CAH-IZO), and Bixbyite In_2O_3 (effective mass calculated at 300 K); optical band gap of amorphous $\text{In}_{0.05}\text{Zn}_{0.38}\text{O}_{0.57}$ extracted by the Tauc plot; optical band gap of crystalline $\text{In}_{0.13}\text{Zn}_{0.28}\text{O}_{0.59}$ extracted by Dolgonos's method; bandgap according to the In/Zn composition ratio; XRR data and fitted simulation of $\text{In}_x\text{Zn}_y\text{O}$ films deposited with different X/Y ratios; density of $\text{In}_x\text{Zn}_y\text{O}$ films according to X/Y ratios of $\text{In}_{0.05}\text{Zn}_{0.38}\text{O}_{0.57}$, $\text{In}_{0.13}\text{Zn}_{0.28}\text{O}_{0.59}$, $\text{In}_{0.17}\text{Zn}_{0.23}\text{O}_{0.60}$, and $\text{In}_{0.25}\text{Zn}_{0.12}\text{O}_{0.63}$ (PDF)

AUTHOR INFORMATION

Corresponding Authors

Sung Beom Cho – Department of Materials Science and Engineering and Department of Energy Systems Research, Ajou University, Suwon 16499, Republic of Korea; orcid.org/0000-0002-3151-0113; Email: csb@ajou.ac.kr

Jin-Seong Park – Division of Materials Science and Engineering, Hanyang University, Seoul 04763, Republic of Korea; orcid.org/0000-0002-9070-5666; Email: jsparklime@hanyang.ac.kr

Authors

TaeHyun Hong – Division of Materials Science and Engineering, Hanyang University, Seoul 04763, Republic of Korea

Hyeon Woo Kim – Division of Materials Science and Engineering, Hanyang University, Seoul 04763, Republic of Korea; Center of Materials Digitalization, Korea Institute of Ceramic Engineering and Technology (KICET), Jinju 52851, Republic of Korea

Yoon-Seo Kim – Division of Materials Science and Engineering, Hanyang University, Seoul 04763, Republic of Korea

Hyun-Jun Jeong – R&D Center, Samsung Display, Yongin 17113, Republic of Korea

Complete contact information is available at:

<https://pubs.acs.org/10.1021/acs.chemmater.3c00894>

Author Contributions

#T.H.H. and H.W.K. contributed equally to this paper.

Notes

The authors declare no competing financial interest.

ACKNOWLEDGMENTS

The computational resources were provided by the Korea Supercomputing Center (KSC-2022-CRE-0352).

REFERENCES

- (1) Sun, W.; Dacek, S. T.; Ong, S. P.; Hautier, G.; Jain, A.; Richards, W. D.; Gamst, A. C.; Persson, K. A.; Ceder, G. The Thermodynamic Scale of Inorganic Crystalline Metastability. *Sci. Adv.* **2016**, *2*, No. e1600225.
- (2) Aykol, M.; Dwaraknath, S. S.; Sun, W.; Persson, K. A. Thermodynamic Limit for Synthesis of Metastable Inorganic Materials. *Sci. Adv.* **2018**, *4*, eaqq0148.
- (3) Stein, A.; Keller, S. W.; Mallouk, T. E. Turning down the Heat: Design and Mechanism in Solid-State Synthesis. *Science* **1993**, *259*, 1558–1564.
- (4) Gopalakrishnan, J. Chimie douce approaches to the synthesis of metastable oxide materials. *Chem. Mater.* **1995**, *7*, 1265–1275.
- (5) Lei, Z.; Yang, X.; Dong, J.; Yi, X. Novel Metastable Hexagonal MoO₃ Nanobelts: Synthesis, Photochromic, and Electrochromic Properties. *Chem. Mater.* **2009**, *21*, 5681–5690.
- (6) Mao, W. L.; Lin, Y. Making the Most of Metastability. *Science* **2022**, *377*, 814–815.
- (7) Sun, W.; Holder, A.; Orváñanos, B.; Arca, E.; Zakutayev, A.; Lany, S.; Ceder, G. Thermodynamic Routes to Novel Metastable Nitrogen-Rich Nitrides. *Chem. Mater.* **2017**, *29*, 6936–6946.
- (8) Holder, A. M.; Siol, S.; Ndione, P. F.; Peng, H.; Deml, A. M.; Matthews, B. E.; Schelhas, L. T.; Toney, M. F.; Gordon, R. G.; Tumas, W.; Perkins, J. D.; Ginley, D. S.; Gorman, B. P.; Tate, J.; Zakutayev, A.; Lany, S. Novel Phase Diagram Behavior and Materials Design in Heterostructural Semiconductor Alloys. *Sci. Adv.* **2017**, *3*, e1700270.
- (9) Amsler, M.; Hegde, V. I.; Jacobsen, S. D.; Wolverton, C. Exploring the High-Pressure Materials Genome. *Phys. Rev. X* **2018**, *8*, 41021.
- (10) Noh, J.; Kim, J.; Stein, H. S.; Sanchez-Lengeling, B.; Gregoire, J. M.; Aspuru-Guzik, A.; Jung, Y. Inverse Design of Solid-State Materials via a Continuous Representation. *Matter* **2019**, *1*, 1370–1384.
- (11) Oganov, A. R.; Pickard, C. J.; Zhu, Q.; Needs, R. J. Structure Prediction Drives Materials Discovery. *Nat. Rev. Mater.* **2019**, *4*, 331–348.
- (12) McDermott, M. J.; Dwaraknath, S. S.; Persson, K. A. A Graph-Based Network for Predicting Chemical Reaction Pathways in Solid-State Materials Synthesis. *Nat. Commun.* **2021**, *12*, 3097.
- (13) Wang, Y.; Liu, J.; Song, Y.; Yu, J.; Tian, Y.; Robson, M. J.; Wang, J.; Zhang, Z.; Lin, X.; Zhou, G.; Wang, Z.; Shen, L.; Zhao, H.; Grasso, S.; Ciucci, F. High-Entropy Perovskites for Energy Conversion and Storage: Design, Synthesis, and Potential Applications. *Small Methods* **2023**, *7*, 2201138.
- (14) Sun, W.; Kitchev, D. A.; Kramer, D.; Ceder, G. Non-Equilibrium Crystallization Pathways of Manganese Oxides in Aqueous Solution. *Nat. Commun.* **2019**, *10*, 573.
- (15) Miura, A.; Ito, H.; Bartel, C. J.; Sun, W.; Rosero-Navarro, N. C.; Tadanaga, K.; Nakata, H.; Maeda, K.; Ceder, G. Selective Metathesis Synthesis of MgCr₂S₄ by Control of Thermodynamic Driving Forces. *Mater. Horiz.* **2020**, *7*, 1310–1316.
- (16) Shi, J.; Zhang, J.; Yang, L.; Qu, M.; Qi, D. C.; Zhang, K. H. L. Wide Bandgap Oxide Semiconductors: From Materials Physics to Optoelectronic Devices. *Adv. Mater.* **2021**, *33*, 2006230.
- (17) Sun, W.; Bartel, C. J.; Arca, E.; Bauers, S. R.; Matthews, B.; Orváñanos, B.; Chen, B. R.; Toney, M. F.; Schelhas, L. T.; Tumas, W.; Tate, J.; Zakutayev, A.; Lany, S.; Holder, A. M.; Ceder, G. A Map of the Inorganic Ternary Metal Nitrides. *Nat. Mater.* **2019**, *18*, 732–739.
- (18) Johnson, R. W.; Hultqvist, A.; Bent, S. F. A Brief Review of Atomic Layer Deposition: From Fundamentals to Applications. *Mater. Today* **2014**, *17*, 236–246.
- (19) Sheng, J.; Lee, J.-H.; Choi, W.-H.; Hong, T.; Kim, M.; Park, J.-S. Review Article: Atomic Layer Deposition for Oxide Semiconductor Thin Film Transistors: Advances in Research and Development. *J. Vac. Sci. Technol., A* **2018**, *36*, No. 060801.
- (20) Wheeler, V. D.; Nepal, N.; Boris, D. R.; Qadri, S. B.; Nyakiti, L. O.; Lang, A.; Koehler, A.; Foster, G.; Walton, S. G.; Eddy, C. R.; Meyer, D. J. Phase Control of Crystalline Ga₂O₃ Films by Plasma-Enhanced Atomic Layer Deposition. *Chem. Mater.* **2020**, *32*, 1140–1152.
- (21) Fortunato, E.; Barquinha, P.; Martins, R. Oxide Semiconductor Thin-Film Transistors: A Review of Recent Advances. *Adv. Mater.* **2012**, *24*, 2945–2986.
- (22) Nomura, K.; Ohta, H.; Takagi, A.; Kamiya, T.; Hirano, M.; Hosono, H. Room-Temperature Fabrication of Transparent Flexible Thin-Film Transistors Using Amorphous Oxide Semiconductors. *Nature* **2004**, *432*, 488–492.
- (23) Lo, C. C.; Hsieh, T. E. Preparation of IGZO Sputtering Target and Its Applications to Thin-Film Transistor Devices. *Ceram. Int.* **2012**, *38*, 3977–3983.
- (24) Koo, J. S.; Lee, D. H.; Yun, S. J.; Jeong, W. C.; Park, J. Y.; Kim, J. W. Development of 65' 4K UHD OLED TV with High Reliability and Short Channel IGZO TFTs. *Proceedings of the International Display Workshops* **2017**, *1*, 439–440.
- (25) Ebata, K.; Tomai, S.; Tsuruma, Y.; Itsuka, T.; Matsuzaki, S.; Yano, K. High-Mobility Thin-Film Transistors with Polycrystalline In-Ga-O Channel Fabricated by DC Magnetron Sputtering. *Appl. Phys. Express* **2012**, *5*, 3–6.
- (26) Goñalves, G.; Barquinha, P.; Pereira, L.; Franco, N.; Alves, E.; Martins, R.; Fortunato, E. High Mobility A-IGO Films Produced at Room Temperature and Their Application in TFTs. *Electrochim. Solid-State Lett.* **2009**, *13*, 20–23.
- (27) Rabbi, M. H.; Lee, S.; Sasaki, D.; Kawashima, E.; Tsuruma, Y.; Jang, J. Polycrystalline InGaO Thin-Film Transistors with Coplanar Structure Exhibiting Average Mobility of ≈78 Cm² V⁻¹ s⁻¹ and Excellent Stability for Replacing Current Poly-Si Thin-Film

- Transistors for Organic Light-Emitting Diode Displays. *Small Methods* **2022**, *6*, No. 2200668.
- (28) Park, J. S.; Sheng, J.; Han, J. H.; Choi, W. H.; Park, J. Performance and Stability Enhancement of In-Sn-Zn-O TFTs Using SiO₂ Gate Dielectrics Grown by Low Temperature Atomic Layer Deposition. *ACS Appl. Mater. Interfaces* **2017**, *9*, 42928–42934.
- (29) Kim, G.-B.; On, N.; Kim, T.; Choi, C. H.; Hur, J. S.; Lim, J. H.; Jeong, J. K. High Mobility IZTO Thin-Film Transistors Based on Spinel Phase Formation at Low Temperature through a Catalytic Chemical Reaction. *Small Methods* **2023**, 2201522.
- (30) Park, B.; Kim, M.; Kang, Y.; Park, H.-B.; Kim, M.-G.; Park, S. K.; Kim, Y.-H. Highly Reliable Implementation of Optimized Multicomponent Oxide Systems Enabled by Machine Learning-Based Synthetic Protocol. *Small Methods* **2021**, *5*, No. 2101293.
- (31) Kim, D.; Nam, T.; Park, J.; Gatineau, J.; Kim, H. Growth Characteristics and Properties of Indium Oxide and Indium-Doped Zinc Oxide by Atomic Layer Deposition. *Thin Solid Films* **2015**, *587*, 83–87.
- (32) Hsu, C. C.; Tsao, C. C.; Chen, Y. H.; Zhang, X. Z. Bipolar Resistive Switching Characteristics of a Sol-Gel InZnO Oxide Semiconductor. *Phys. B* **2019**, *S61*, 64–69.
- (33) Sheng, J.; Lee, H. J.; Oh, S.; Park, J. S. Flexible and High-Performance Amorphous Indium Zinc Oxide Thin-Film Transistor Using Low-Temperature Atomic Layer Deposition. *ACS Appl. Mater. Interfaces* **2016**, *8*, 33821–33828.
- (34) Tomai, S.; Terai, K.; Junke, T.; Tsuruma, Y.; Ebata, K.; Yano, K.; Uraoka, Y. The Electrical Conduction Properties of Poly-Crystalline Indium-Zinc-Oxide Film. *J. Appl. Phys.* **2014**, *115*, No. 083701.
- (35) Kim, H.; Choi, D.; Park, S.; Park, K.; Park, H. W.; Chung, K. B.; Kwon, J. Y. Impact of Bias Stability for Crystalline InZnO Thin-Film Transistors. *Appl. Phys. Lett.* **2017**, *110*, 232104.
- (36) Hautier, G.; Fischer, C.; Ehrlacher, V.; Jain, A.; Ceder, G. Data Mined Ionic Substitutions for the Discovery of New Compounds. *Inorg. Chem.* **2011**, *50*, 656–663.
- (37) Belkly, A.; Helderman, M.; Karen, V. L.; Ulkch, P. New Developments in the Inorganic Crystal Structure Database (ICSD): Accessibility in Support of Materials Research and Design. *Acta Crystallogr., B* **2002**, *58*, 364–369.
- (38) Jain, A.; Ong, S. P.; Hautier, G.; Chen, W.; Richards, W. D.; Dacek, S.; Cholia, S.; Gunter, D.; Skinner, D.; Ceder, G.; Persson, K. A. Commentary: The Materials Project: A Materials Genome Approach to Accelerating Materials Innovation. *APL Mater.* **2013**, *1*, No. 011002.
- (39) Madsen, G. K. H.; Carrete, J.; Verstraete, M. J. BoltzTraP2, a Program for Interpolating Band Structures and Calculating Semi-Classical Transport Coefficients. *Comput. Phys. Commun.* **2018**, *231*, 140–145.
- (40) Nomura, K.; Ohta, H.; Ueda, K.; Kamiya, T.; Hirano, M.; Hosono, H. Thin-Film Transistor Fabricated in Single-Crystalline Transparent Oxide Semiconductor. *Science* **2003**, *300*, 1269–1272.
- (41) Jeong, H. J.; Kim, Y. S.; Jeong, S. G.; Park, J. S. Impact of Annealing Temperature on Atomic Layer Deposited In-Ga-Zn-O Thin-Film Transistors. *ACS Appl. Electron. Mater.* **2022**, *4*, 1343–1350.
- (42) On, N.; Kim, B. K.; Kim, Y.; Kim, E. H.; Lim, J. H.; Hosono, H.; Kim, J.; Yang, H.; Jeong, J. K. Boosting Carrier Mobility and Stability in Indium–Zinc–Tin Oxide Thin-Film Transistors through Controlled Crystallization. *Sci. Rep.* **2020**, *10*, 18868.
- (43) Buell, C. H.; Shuck, F. O. *Determination of liquid metal diffusion coefficients by molecular distillation. No. IS-132S*; Ames Lab., Iowa State Univ. of Science and Tech.: IA (USA), 1966.
- (44) Koch, C. T. Determination of core structure periodicity and point defect density along dislocations. Ph.D., Arizona State University, Phoenix, AZ, 2022.
- (45) Kim, H. W.; Ko, H.; Chung, Y. C.; Cho, S. B. Heterostructural Phase Diagram of Ga₂O₃-Based Solid Solution with Al₂O₃. *J. Eur. Ceram. Soc.* **2021**, *41*, 611–616.
- (46) Pitike, K. C.; Macias, A.; Eisenbach, M.; Bridges, C. A.; Cooper, V. R. Computationally Accelerated Discovery of High Entropy Pyrochlore Oxides. *Chem. Mater.* **2022**, *34*, 1459–1472.
- (47) Zunger, A.; Wei, S.-H.; Ferreira, L. G.; Bernard, J. E. Special Quasirandom Structures. *Phys. Rev. Lett.* **1990**, *65*, 353–356.
- (48) Lee, H. U.; Kim, H. W.; Fatti, G.; Ko, H.; Cho, S. B. Dominant Effects of Epitaxial Strain on the Phase Control of Heterostructural (In_xGa_{1-x})₂O₃Alloys. *ACS Appl. Electron. Mater.* **2022**, *4*, 2711–2717.
- (49) Seacat, S.; Lyons, J. L.; Peelaers, H. Properties of Orthorhombic Ga₂O₃ Alloyed with In₂O₃ and Al₂O₃. *Appl. Phys. Lett.* **2021**, *119*, No. 042104.
- (50) Moriga, T.; Edwards, D. D.; Mason, T. O.; Palmer, G. B.; Poeppelmeier, K. R.; Schindler, J. L.; Kannewurf, C. R.; Nakabayashi, I. Phase Relationships and Physical Properties of Homologous Compounds in the Zinc Oxide-Indium Oxide System. *J. Am. Ceram. Soc.* **1998**, *81*, 1310–1316.
- (51) Yamazaki, S.; Koyama, J.; Yamamoto, Y.; Okamoto, K. Research, Development, and Application of Crystalline Oxide Semiconductor. *Dig. Tech. Pap.* **2012**, *43*, 183–186.
- (52) Glushkova, A. V.; Dekkers, H. F. W.; Nag, M.; Del Agua Borniquel, J. I.; Ramalingam, J.; Genoe, J.; Heremans, P.; Rolin, C. Systematic Study on the Amorphous, C-Axis-Aligned Crystalline, and Protocrystalline Phases in In-Ga-Zn Oxide Thin-Film Transistors. *ACS Appl. Electron. Mater.* **2021**, *3*, 1268–1278.
- (53) Hautier, G.; Miglio, A.; Waroquiers, D.; Rignanese, G. M.; Gonze, X. How Does Chemistry Influence Electron Effective Mass in Oxides? A High-Throughput Computational Analysis. *Chem. Mater.* **2014**, *26*, 5447–5458.
- (54) Kamiya, T.; Hosono, H. Material Characteristics and Applications of Transparent Amorphous Oxide Semiconductors. *NPG Asia Mater.* **2010**, *2*, 15–22.
- (55) Sheng, J.; Hong, T. H.; Lee, H. M.; Kim, K. R.; Sasase, M.; Kim, J.; Hosono, H.; Park, J. S. Amorphous IGZO TFT with High Mobility of 70 Cm²/(V s) via Vertical Dimension Control Using PEALD. *ACS Appl. Mater. Interfaces* **2019**, *11*, 40300–40309.
- (56) Kresse, G.; Furthmüller, J. Efficient Iterative Schemes for Ab Initio Total-Energy Calculations Using a Plane-Wave Basis Set. *Phys. Rev. B: Condens. Matter Mater. Phys.* **1996**, *54*, 11169–11186.
- (57) Kresse, G.; Furthmüller, J. Efficiency of Ab-Initio Total Energy Calculations for Metals and Semiconductors Using a Plane-Wave Basis Set. *Comput. Mater. Sci.* **1996**, *6*, 15–50.
- (58) Blöchl, P. E. Projector Augmented-Wave Method. *Phys. Rev. B* **1994**, *50*, 17953–17979.
- (59) Perdew, J. P.; Burke, K.; Ernzerhof, M. Generalized Gradient Approximation Made Simple. *Phys. Rev. Lett.* **1996**, *77*, 3865–3868.
- (60) Ong, S. P.; Richards, W. D.; Jain, A.; Hautier, G.; Kocher, M.; Cholia, S.; Gunter, D.; Chevrier, V. L.; Persson, K. A.; Ceder, G. Python Materials Genomics (Pymatgen): A Robust, Open-Source Python Library for Materials Analysis. *Comput. Mater. Sci.* **2013**, *68*, 314–319.
- (61) Ricci, F.; Chen, W.; Aydemir, U.; Snyder, G. J.; Rignanese, G. M.; Jain, A.; Hautier, G. Data Descriptor: An Ab Initio Electronic Transport Database for Inorganic Materials. *Sci. Data* **2017**, *4*, 170085.
- (62) Scott Weingarten, N.; Byrd, E. F. C. Special Quasirandom Structures of Alon. *Comput. Mater. Sci.* **2015**, *96*, 312–318.
- (63) Van De Walle, A.; Tiwary, P.; De Jong, M.; Olmsted, D. L.; Asta, M.; Dick, A.; Shin, D.; Wang, Y.; Chen, L. Q.; Liu, Z. K. Efficient Stochastic Generation of Special Quasirandom Structures. *CALPHAD* **2013**, *42*, 13–18.